Optics Letters

InGaAs/GaAs nano-ridge laser with an amorphous silicon grating monolithically grown on a 300 mm Si wafer

Z. Ouyang,[1,*] D. Colucci,[1,2] E. M. B. Fahmy,[1] A. A. Yimam,[1] J. Van Campernhout,[2]
B. Kunert,[1] and D. Van Thourhout[1]

[1]Ghent University-IMEC, Photonics Research Group, INTEC department, iGent, Technologiepark-Zwijnaarde 126, 9052 Ghent, Belgium
[2]IMEC, Kapeldreef 75, 3001 Heverlee, Belgium
*Zhongtao.Ouyang@ugent.be

The monolithic growth of direct-bandgap III–V materials directly on a Si substrate is a promising approach for the fabrication of complex silicon photonic integrated circuits including light sources and amplifiers. It remains challenging to realize practical, reliable, and efficient light emitters due to misfit defect formation during the epitaxial growth. Exploiting nano-ridge engineering (NRE), III–V nano-ridges with high crystal quality were achieved based on aspect ratio defect trapping inside narrow trenches. In an earlier work, we used an etched grating to create distributed feedback lasers from these nano-ridges. Here we deposited an amorphous silicon grating on the top of the nano-ridge. Under pulsed optical pumping, a ~7.84 kW/cm² lasing threshold was observed, ~5 times smaller compared to devices with an etched grating inside the nano-ridge. Compared to the etched grating, the amorphous silicon grating introduces no extra carrier loss channels through surface state defects, which is believed to be the origin of the lower threshold. This low threshold again demonstrates the high quality of the epitaxial deposited material and may provide a route toward further optimizing the electrically driven devices.
 © 2024 Optica Publishing Group. All rights, including for text and data mining (TDM), Artificial Intelligence (AI) training, and similar technologies, are reserved.

Introduction. Leveraging well-developed processes from the complementary metal–oxide–semiconductor (CMOS) industry, silicon photonics circuits incorporating various optical components, including high-efficiency grating couplers, high-response-speed photodetectors, and excellent modulators [1–3], are now widely studied and used in applications. However, the lack of a high-performance laser is a main bottleneck for further development of the silicon photonics platform. Direct-bandgap III–V semiconductors are promising candidates for realizing a practical and compact light source but not easy to integrate on silicon. Several methods, including flip-chip, bonding, transfer printing, and direct monolithic epitaxy of III–V materials utilizing a strain-relaxed buffer layer [4–11], were explored to achieve this but all have their limitations. The novel nano-ridge

engineering (NRE) technique [12–14] has been shown to enable the growth of high-quality III-V material directly on Si substrates with a thin buffer and, compared to other methods, has shown advantages in terms of device scalability, integration density, and cost.

In our previous work, we demonstrated lasing from nano-ridge devices using an etched grating to define the cavity [15]. However, the threshold of these devices was still relatively high. One of the suspected reasons is that the etched structure caused damage to the InGaP passivation layer, which introduces carrier loss paths at the GaAs–air interface and within the GaAs bulk. Hence, it is necessary to avoid such defect formation for improving the laser performance. Therefore, in this work, a high-refractive-index amorphous silicon (aSi) grating was deposited on top of the nano-ridge rather than etching a grating inside the nano-ridge. The design of the aSi grating considered the trade-off between the coupling strength of the grating and the mode overlap with the quantum wells (QWs), resulting in a nano-ridge cavity with low lasing threshold.

In the Design and Fabrication section, the growth process of the proposed III–V nano-ridge, the analysis of the epitaxial material quality through photoluminescence (PL) spectroscopy, the cavity design principle, and the fabrication process flow are described.

In the Result and Discussion section, we demonstrate single-mode lasing for the fabricated devices. Through time-resolved photoluminescence (TRPL), we investigate the impact of etching on the PL lifetime. Finally, we compare the lasing characteristics of the device with similar devices reported earlier.

Design and fabrication. *GaAs nano-ridge epitaxial growth:* The box-shaped nano-ridge lasers are based on fully relaxed GaAs nano-ridges including two compressively strained InGaAs QWs on top of a GaPAs blocking layer. The final InGaP capping layer is wrapped around the entire nano-ridges to suppress surface recombination. These laser structures were grown by metal organic vapor phase epitaxy (MOVPE) on a silicon substrate containing narrow trenches patterned in a SiO₂ layer. Through a combination of aspect ratio trapping (ART) and nano-ridge engineering (NRE), a high nano-ridge crystal quality with a large III–V material volume was obtained. The details of the epitaxy process can be found in previous reports [12–15].
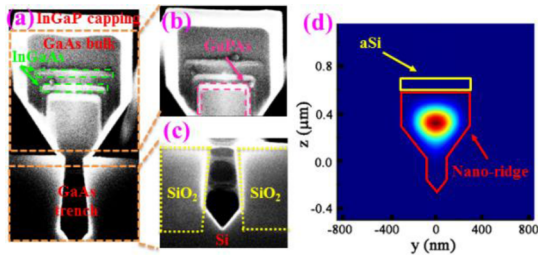
Fig. 1. (a) Cross-sectional SEM image of the nano-ridge structure. (b) Enlarged image of the InGaAs QWs and GaPAs carrier blocking layer. (c) Image of the ART-trench region. (d) Lowest order transverse electric (TE)-like mode for a 539-nm-high and 582-nm-wide nano-ridge with a 100-nm-high aSi grating.

Figures 1(a)–1(c) show the cross-sectional scanning electron microscopy (SEM) images of the overall structure after a 1 min wet etching using a solution consisting of 50% citric acid mixed with 30% hydrogen peroxide at a ratio of 10:1. Due to the increasing thickness contrast with different wet etching rates of the different materials inside the nano-ridge, the InGaP capping layer, the GaAs bulk layer, the InGaAs QWs, the GaPAs carrier blocking layer, and the GaAs trench are clearly visible in Fig. 1(a). In the enlarged SEM image of Fig. 1(b) the GaPAs carrier blocking layer and the QWs are clearly visible. The GaPAs carrier blocking layer confines the carriers above the trench and reduces carrier loss in the trench region [15,16]. Figure 1(c) shows the details of the trench part. Figure 1(d) presents the lowest order transverse electric (TE)-like mode for a 539-nm-high and 582-nm-wide nano-ridge with a 120 nm trench and a 100-nm-high aSi grating on top. The field was calculated using a 3D-finite difference time domain (3D-FDTD) simulation with Bloch boundary conditions, assuming a 50% duty cycle for the grating and with the cross section taken in the high-index region.

Photoluminescence: The material quality of the nano-ridge was characterized by PL measurements at room temperature (R.T.). The nano-ridges were excited from the top by a 532 nm continuous-wave (CW) solid-state diode laser. The emission scattered from the nano-ridges was collected from the top and detected with a monochromator and a thermo-electric-cooled InGaAs detector, as previous reports [15]. Figure 2(a) presents the normalized PL spectrum from nano-ridges with different trench sizes under a 4.20 W/cm² pumping power density. The PL spectrum contains a broad peak extending from 1000 nm to 1060 nm. The redshift in the PL peak with increasing trench width can be explained by the change of indium concentration and/or QW thickness, which induces a shift in the energy of the quantized states. Both effects are likely to take place because the epitaxy is sensitive to local growth conditions, which change due to the fixed fill-factor in the oxide-trench pattern. The cavity design discussed in the next section targets this wavelength region.

Laser design Next, single-mode distributed feedback (DFB) lasers incorporating a $\lambda/4$ phase shift were designed using a 3D-FDTD solver. The simulated device model is shown in the inset of Fig. 2(b). The grating duty cycle was fixed to 50% and the period of the aSi grating (Λ) was chosen to match the cavity resonance with the PL peak. From here on, we focus on a 539-nm-high and 582-nm-wide nano-ridge with a 120 nm trench, as their wider top surface makes the fabrication of the aSi grating easier compared to the nano-ridges with trench sizes
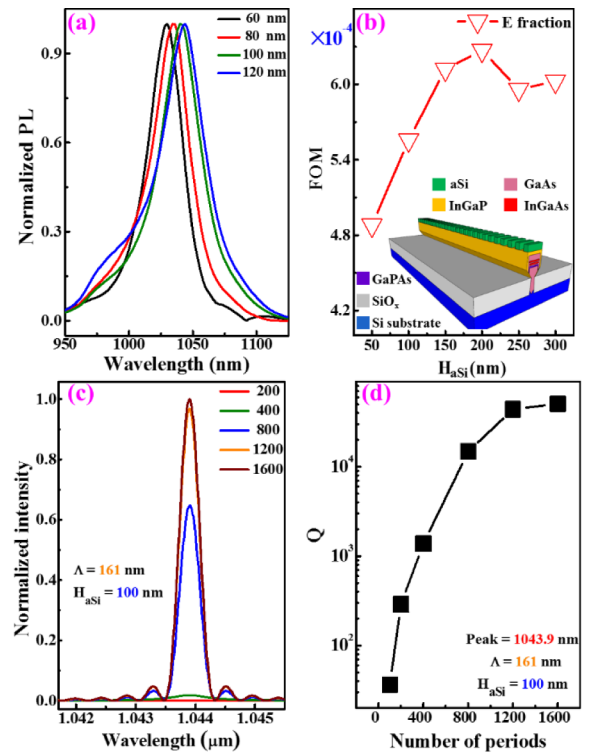

Fig. 2. (a) PL spectrum from nano-ridges with 60, 80, 100, and 120 nm trench widths under a 4.20 W/cm² 532 nm continuous-wave pumping. (b) Dependence of FOM on H_{aSi}. (c) Simulated spectrum from the nano-ridge with $H_{aSi} = 100$ nm and increasing number of periods. (d) Quality factor versus number of periods.

of 60, 80, and 100 nm. To optimize the trade-off between the light interaction with the grating and the mode confinement in the QWs, the height of the aSi grating (H_{aSi}) was varied in the simulation. As the figure of merit (FOM), we choose the product $\Gamma_{QW}\Gamma_{aSi}$, with Γ_{QW} the ratio of the integrated electric field intensity in the QWs to the one in the whole simulation region and Γ_{aSi} the similar ratio, but for the aSi grating. The simulation was performed with Bloch boundary conditions using a 3D-FDTD solver. Figure 2(b) shows the result for a nano-ridge device as a function of H_{aSi}. The FOM first increases and then decreases with increasing H_{aSi}, which is ascribed to a shift of the lasing mode to the thicker high-index aSi grating. Although the FOM reaches a maximum when $H_{aSi} = 200$ nm, experimentally we found that grating teeth higher than 100 nm tended to bend and touch each other after processing, due to the high aspect ratio. Thus, from here on, we mostly focus on devices with $H_{aSi} = 100$ nm, taking both the height optimization and process tolerances into account.

Figure 2(c) shows simulated spectra for nano-ridge devices with aSi gratings with $\Lambda = 161$ nm and different cavity lengths. For devices with 800 and more periods in total, the strength of the resonance peak strongly increases, indicating that in this case the grating provides sufficient reflection to form a cavity.

Figure 2(d) plots the simulated quality factor (Q-factor) as a function of the number of periods. The Q-factor increases with increasing number of periods due to the reduction of the light leaking at the beginning and end of the grating. Above 800 periods, the Q-factor starts to stabilize because other leakage mechanisms become more important. Therefore, in our final
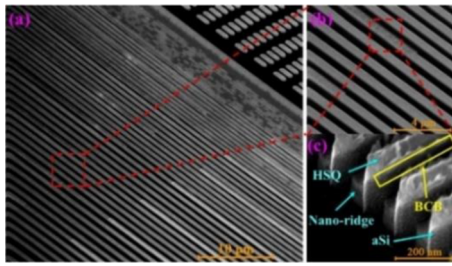
Fig. 3. (a) Tilted SEM image of DFB lasers with 60, 80, 100, and 120 nm trench widths. (b) Zoomed-in image of the region with the first-order grating on a 539-nm-high and 582-nm-wide nano-ridge. (c) Zoomed-in image of the grating.

design, we choose a grating with 800 periods and $H_{aSi} = 100$ nm, to achieve a low threshold device. A second-order grating coupler with 200 periods was added at each side of the nano-ridge cavity to facilitate device characterization.

Fabrication process: The aSi film was deposited on the nano-ridge chips by plasma-enhanced chemical vapor deposition (PECVD) after acetone, isopropyl alcohol (IPA), and DI water cleaning. A ~50 nm cured BCB (benzocyclobutene) layer was added as a protection layer before spin coating a ~150 nm HSQ (hydrogen silsesquioxane) electron beam resist. This protection layer is critical given the reaction between the aSi layer and the HSQ developer (AZ400K:DI water = 1:3). Then, gratings with 800 periods were patterned using electron beam lithography (EBL) into the HSQ resist. The patterned structures were transferred from the HSQ resist to the aSi layer by reactive ion etching of the BCB layer and the aSi layer with SF_6/O_2 and $CF_4/H_2/SF_6$, respectively. Figure 3(a) shows a tilted SEM view of the fabricated devices with the 200 period second-order gratings clearly visible at the bottom-right corner. Figure 3(b) is a zoomed-in image of the region with the first-order grating and Fig. 3(c) shows that the sidewalls of the aSi grating are vertical.

Result and discussion. The devices were excited by a Nd:YAG 532 nm nanosecond pulsed laser (7 ns pulse width, 938 HZ repetition rate) at room temperature. The emission from the devices was collected and detected with the same monochromator and InGaAs detector, as mentioned before. Figure 4(a) shows a microscope picture of a full array of devices excited simultaneously by a pumping spot with a Gaussian profile and a full width at half maximum of 400 μm. To characterize the individual devices, a rectangle aperture was utilized to control the pumping shape, as shown in Fig. 4(b). Figure 4(c) shows the PL spectrum from the DFB laser having an aSi grating with $H_{aSi} = 100$ nm and $\Lambda = 161$ nm, under different power densities. The 1044 nm lasing peak becomes apparent when the pumping density reaches 2.5 kW/cm², and the peak intensity increases strongly with the further increase of the pumping density. At a pumping density of 35 kW/cm², the lasing peak reaches a side-mode suppression ratio of more than 35 dB. The linewidth of the laser, obtained from a Gaussian function fitting as shown in the inset, is 1.5 nm and likely limited by the pulsed .operating regime

Figure 4(d) shows the light in (pumping power density)–light out (integrated PL) curve on a logarithm and a linear (inset) scale for the same measured laser. A clear change of slope is a signature of the lasing turn-on. The threshold density is 7.84 kW/cm², obtained from the second-order derivative of the light in–light out curve on the linear scale [17]. This threshold is ~5 times
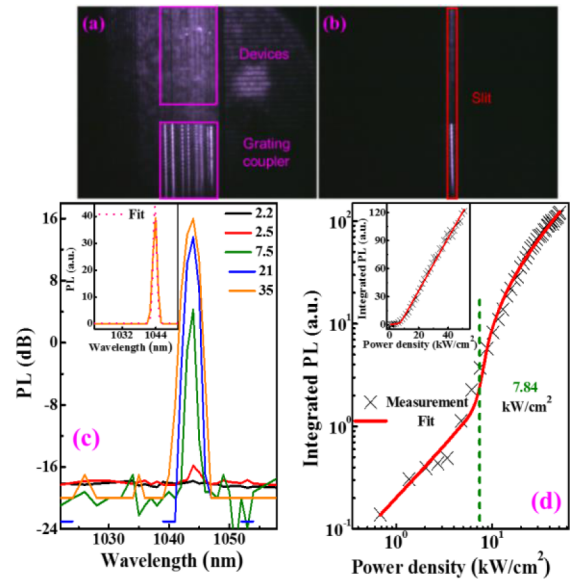

Fig. 4. (a) Microscope image of a full array of devices excited simultaneously by a 532 nm pulsed pumping. (b) Microscope image of one excited DFB laser with rectangular aperture. (c) PL spectrum from the DFB laser under 2.2, 2.5, 7.5, 21, and 35 kW/cm² pulsed pumping power densities. Inset: PL spectrum on a linear scale with a Gaussian function fitting from the same DFB laser under 35 kW/cm². (d) Light in–light out curve on logarithmic and linear (inset) scales of the same DFB laser.

smaller than the value for the nano-ridge with an etched grating (33.4 kW/cm²) [15]. The light in–light out curve on both linear and log scales are fitted to the rate equations [18,19] giving a value β ~ 0.9% for the coupling efficiency from the spontaneous emission to the cavity mode. In theory, a higher β value is beneficial to obtain a lower lasing threshold value. However, the β value is almost the same as for the nano-ridge laser with an etched grating. Thus, the coupling efficiency β is not the main reason for the lower lasing turn-on threshold value. Note that in principle the coupling efficiency β could be improved by optimizing the nano-ridge dimensions. Simulations show that this leads to a strongly reduced overall cross section, which is not necessarily favorable in terms of the overall laser design and might, e.g., lead to considerably lower output powers.

To better understand the origin of the lowered threshold, TRPL measurements were carried out, as these can provide insight in extra carrier losses introduced by an etched grating at the GaAs–air surfaces and in the QWs. The nano-ridges were excited by a Ti:sapphire ultrafast laser (35 fs pulse width, 8 MHZ repetition rate) at both room temperature (R.T.) and cryogenic temperature (Cryo., 5 K). The emission from the nano-ridges was collected and detected with a monochromator and a superconducting nanowire single-photon detector.

Figure 5(a) presents the decay curve for the room temperature emission at 1044 nm from a nano-ridge with and without etching. Both samples went through the same process steps, but a thicker BCB layer was used in the "Unetched" nano-ridge to protect the material from being etched. A single exponential decay function is utilized for fitting. The fitted lifetime of the etched nano-ridge is five times smaller than the one without, 76 ps compared to 379 ps. This is consistent with the reduction in pumping threshold for the lasers with an aSi grating versus those with an etched grating (5×) [15].
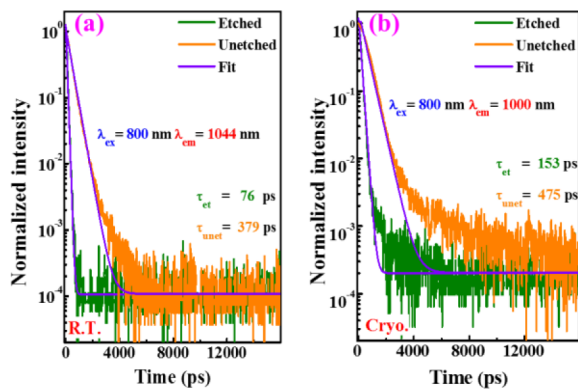
Fig. 5. Decay traces of the 1044 nm and 1000 nm emission from nano-ridges with and without etching under an 800 nm pulsed pumping at (a) room temperature and (b) cryogenic temperature.

To further investigate the origin of the decreased lifetime, the measurements were repeated at cryogenic temperature (5 K); see Fig. 5(b). At this temperature, the carriers are expected to have insufficient thermal energy to escape the InGaAs QWs, and hence the measured lifetime only depends on the material quality of the QWs, and not on the surface defects. The lifetime for the nano-ridge with etched grating is now 153 ps, double that of the one at room temperature, but still smaller than the one without etching (379 ps and 475 ps at room temperature and cryogenic temperature, respectively). This demonstrates that the etching introduces extra carrier loss paths. In summary, we believe that the decreased lifetime for the devices with etched grating originates both from surface non-radiative recombination centers at the GaAs-air interface, which is exposed by etching the InGaP passivation layer [16], and by defects introduced in the QWs by the high-impact ions used in the plasma etching process.

Previously, we reported InP [20] and InGaAs/InP [21] DFB lasers with etched gratings exhibiting laser thresholds of 2143 kW/cm^2 and 760 kW/cm^2. The DFB laser reported here, with an aSi grating on top, demonstrates a threshold of 7.84 kW/cm^2, more than two orders of magnitude lower. This superior performance can be attributed to the following reasons: 1) the incorporation of an extra InGaP passivation layer suppressing non-radiative recombination via surface states, 2) the absence of damage to the nano-ridge material during aSi grating fabrication, and 3) enhanced carrier confinement inside the QW layers. Leveraging ART and lateral ART techniques, Han *et al.* reported InP Fabry–Perot (FP) lasers, distributed Bragg reflector (DBR) lasers, and DFB lasers with an etched grating on the two sides [8,22–24]. These devices had a lasing threshold ranging from 16 µJ/cm^2 to 40 µJ/cm^2. In this case, ultrashort pulses (100 fs) were used, making a direct comparison not straightforward. In contrast, given that the 7 ns pumping pulse width used here is much larger than the measured lifetime, the DFB laser with aSi grating can be considered to lase under quasi-continuous pumping conditions.

Recently, also an electrically driven nano-ridge laser was demonstrated [25]. Also for these lasers, incorporating a grating would be beneficial to enhance single-mode lasing and mode stability. Similar as we demonstrated here, using an amorphous silicon grating rather than an etched grating will be beneficial to keep the laser threshold low. Combining such a grating with the electrical injection scheme developed in Ref. [25] will require further developments, however.

Conclusion. In conclusion, a 100-nm-high, 161-nm-period aSi grating with 800 periods was integrated on top of a GaAs nano-ridge directly grown on a standard 300 mm Si wafer. This approach allowed to demonstrate lasing with strongly lowered threshold compared to the device with an etched grating, which suffers from additional non-radiative recombination, and compared to the devices with a metal grating on top, which suffers from increased propagation losses. The room temperature photoluminescence spectrum shows a single-mode laser operation with more than 35 dB side-mode suppression ratio and 7.84 kW/cm^2 lasing threshold. This lasing threshold is ∼5 times smaller than for a DFB laser with a grating etched into the nano-ridge. This is ascribed to the fact that the aSi grating fabrication process allows to avoid extra carrier loss paths from surface-state defects at the GaAs–air interface and from damage in the quantum wells' active region due to the high-energy ions involved in the plasma process used for the etched gratings. This demonstration of a nano-ridge laser with low threshold proves the high quality of the III–V-on-silicon epitaxial material again and opens up the road toward further improving the performance of electrically driven devices.

Disclosures. The authors declare no conflicts of interest.

Data availability. Data underlying the results presented in this paper are not publicly available at this time but may be obtained from the authors upon reasonable request.

REFERENCES

1. R. Marchetti, C. Lacava, A. Khokhar, *et al.*, Sci. Rep. **7**, 16670 (2017).
2. N. Youngblood, C. Chen, S. J. Koester, *et al.*, Nat. Photonics **9**, 247 (2015).
3. Y. Terada, K. Kondo, R. Abe, *et al.*, Opt. Lett. **42**, 5110 (2017).
4. H. Lu, J. S. Lee, Y. Zhao, *et al.*, Opt. Express **24**, 16258 (2016).
5. T. Aihara, T. Hiraki, K. Takeda, *et al.*, Opt. Express **27**, 36438 (2019).
6. J. Zhang, G. Muliuk, J. Juvert, *et al.*, APL Photonics **4**, 110803 (2019).
7. S. Chen, W. Li, J. Wu, *et al.*, Nat. Photonics **10**, 307 (2016).
8. Y. Xue, J. Li, Y. Wang, *et al.*, Laser Photonics Rev. **18**, 2300549 (2024).
9. A. Y. Liu, J. Peters, X. Huang, *et al.*, Opt. Lett. **42**, 338 (2017).
10. H. Schmid, M. Borg, K. Moselund, *et al.*, Appl. Phys. Lett. **106**, 233101 (2015).
11. Y. Kawaguchi, K. Murakawa, M. Usagawa, *et al.*, Cryst. Growth Des. **23**, 3572 (2023).
12. M. Baryshnikova, Y. Mols, Y. Ishii, *et al.*, Crystals **10**, 330 (2020).
13. D. Van Thourhout, Y. Shi, Baryshnikova, *et al.*, Semicond. Semimetals **101**, 283 (2019).
14. D. Colucci, M. Baryshnikova, Y. Shi, *et al.*, Opt. Express **30**, 13510 (2022).
15. Y. Shi, Z. Wang, J. Van Campenhout, *et al.*, Optica **4**, 1468 (2017).
16. Y. Shi, L. C. Kreuzer, N. C. Gerhardt, *et al.*, J. Appl. Phys. **127**, 103104 (2020).
17. C. Z. Ning, IEEE J. Select. Topics Quantum Electron. **19**, 1503604 (2013).
18. H. Yokoyama and S. D. Brorson, J. Appl. Phys. **66**, 4801 (1989).
19. K. A. Shore and M. Ogura, Opt. Quantum Electron. **24**, S209 (1992).
20. Z. Wang, B. Tian, M. Pantouvaki, *et al.*, Nat. Photonics **9**, 837 (2015).
21. B. Tian, Z. Wang, M. Pantouvaki, *et al.*, Nano Lett. **17**, 559 (2017).
22. Y. Han, W. K. Ng, Y. Xue, *et al.*, Opt. Lett. **44**, 767 (2019).
23. Y. Han, W. K. Ng, Y. Xue, *et al.*, Photonics Res. **7**, 1081 (2019).
24. Y. Han, Z. Yan, W. K. Ng, *et al.*, Optica **7**, 148 (2020).
25. Y. De Koninck, C. Caer, D. Yudistira, *et al.*, "GaAs nano-ridge laser diodes fully fabricated in a 300 mm CMOS pilot line," arXiv (2023).